KSME

Springer

Journal of Mechanical Science and Technology 34 (6) 2020

Original Article
DOI 10.1007/s12206-020-0518-4

Keywords:
· Variable nozzle turbine
· Nozzle leakage flow
· Solidity
· Thickness
· Shock

Correspondence to:
Dazhong Lao
laodazhong@tsinghua.org.cn

Citation:
Yang, D., Cao, L., Yang, C., Lao, D., Sun, H. (2020). Investigations on the effect of guide vane thickness and solidity on shock and unsteady flow characteristic of VNT. Journal of Mechanical Science and Technology 34 (6) (2020) 2423~2433. http://doi.org/10.1007/s12206-020-0518-4

Received October 20th, 2019
Revised February 20th, 2020
Accepted March 15th, 2020

† Recommended by Editor Yang Na

Investigations on the effect of guide vane thickness and solidity on shock and unsteady flow characteristic of VNT

Dengfeng Yang[1], Li'ang Cao[1], Ce Yang[2], Dazhong Lao[3] and Harold Sun[4,5]

[1]School of Control Engineering, Northeastern University at Qinhuangdao, Qinhuangdao 066004, China, [2]School of Mechanical Engineering, Beijing Institute of Technology, Beijing 100081, China, [3]School of Aerospace Engineering, Beijing Institute of Technology, Beijing 100081, China, [4]School of Mechanical Engineering, Tianjin University, Tianjin 300072, China, [5]R&D Center Detroit, GAC, Michigan 48124, USA

Abstract In this work, the influence of thickness and solidity of guide vane on the unsteady flow of a radial inflow turbine with variable nozzle has been numerically studied. Three vanes with the thickness changes from 0.3 to 0.1 and the solidity changes from 1.43 to 2.86, were chosen for this study. By investigating the unsteady flow field, it is found that the vane with low thickness and high solidity (vane B) can reduce shock by 75 % compared to the vane with high thickness and low solidity (base model); meanwhile, it can also mitigate the nozzle end-wall leakage flow thus improves the flow uniformity of rotor inlet. As the intensity of shock and nozzle leakage flow were mitigated, the aerodynamic loading fluctuation of rotor blade can be weakened effectively, which will lead to improved rotor blades forced response. However, at small opening, vane B shows about 0.5 % lower efficiency than the base model; at large open condition, the efficiency degradation of vane B is up to 1.4 %. Therefore, there is a trade-off between the efficiency and forced response when choosing the nozzle vane solidity and thickness.

1. Introduction

Over the last decades, variable nozzle turbines (VNTs) have been widely applied to turbochargers in order to improve engine low-speed torque and transient response [1, 2]. The variable nozzle, as a main part of the VNT, relies on pivoting guide vanes to adjust turbine's mass flow rate (MFR) [3]. When engine works at exhaust braking condition, variable nozzle generally works at small openings. In this case, the large setting angle of guide vane with the low ratio of nozzle throat width to vane height can substantially increase the percentage of nozzle leakage flow rate, leading to a large efficiency loss [4, 5]. Some papers highlighted the characteristics of nozzle leakage flow by both experimental and CFD methods. Tamaki et al. [6] undertook a comprehensive investigation of the effect of nozzle leakage flow on turbine performance at different nozzle openings. The results showed that nozzle leakage flow can seriously distort the flow field at small nozzle openings, thus result in turbine efficiency penalty; while at large nozzle openings, the effect of nozzle leakage flow is negligible.

Hu et al. [7] investigated the effect of nozzle clearance height on turbine performance and the results show that turbine stage efficiency will decrease as the increase of clearance height. Spence et al. [8] and Walkingshaw et al. [9] investigated the nozzle leakage flow characteristics and found that the characteristics of the leakage flow varied considerably with guide vane position, but not with turbine operating condition.

The nozzle leakage flow interacted with the main flow, producing vortices, which causes flow loss and disrupts the flow at nozzle exit. Qiu et al. [10] claimed that at rotor inlet position, the nozzle clearance leakage flow has higher radial velocity compared with main flow, thus the flow at the rotor inlet cannot be turned sufficiently, resulting in decrease of exhaust gas work capacity. The study of Hayami et al. [11] revealed that flow field of rotor inlet area can be significantly

affected by nozzle leakage flow when a rotor has fewer blades; however, as the blade number increases, the impact of nozzle leakage flow will be reduced. In addition to the effect of nozzle leakage flow on turbine performance [7]. Hu et al. [12] also investigated the rotor blade forced response caused by nozzle leakage flow, using unsteady numerical methods. The results indicated that nozzle leakage flow can lead to high aerodynamic loading fluctuation on rotor leading edge thus directly affect the durability of rotor blades. Similar results are given in a series of publications by Liu et al. [13] and Kulkarni and Larue [14], based on CFD/CAE methods.

Some papers studied the influence of guide vane thickness and solidity on turbine performance and unsteady flow characteristics by both experimental and CFD methods. Simpson [15] carried out a series of test on a 135 mm tip diameter radial turbine using a variety of stator designs and found that increases the values of the guide vane thickness will lead to a reduction in the amplitudes of the measured and predicted static pressure variations at the rotor inlet, thus affects the performance of turbine. The study by Yang et al. [16] showed that the nozzle leakage flow and shock intensity can directly be affected by nozzle solidity and thickness, but the study did not give quantitative results. Qi et al. [17] investigated the nozzle leakage flow and shock under the varying expansion ratio of turbine, however, the study was only performed on a high thickness and low solidity guide vane. Ben studied the shock intensity under different nozzle clearance size, results shown that an optimal distribution of the nozzle endwall clearance can improve turbine efficiency and shift nozzle trailing edge shock [18].

In the design of VNT, it has been a major challenge to prevent the shock from being generated as the exhaust gas can easily be accelerated to supersonic when turbine works at small nozzle opening with high expansion ratio conditions. Chen [19] found that a shock can be induced at engine exhaust braking conditions, and impinge on downstream rotor blades periodically, thus damage the VNT. Kawakubo [20] investigated the interaction between shock and downstream rotor blades, indicating that shock could lead to highly alternating load on the rotor leading edge, thus induce vibration of the rotor blades. Yang et al. [21] studied the acceleration process of exhaust gas using CFD methods and found that shock could be mitigated effectively by reducing the shrinkage degree of the acceleration channel in nozzle. The investigation of Feneley et al. [22] also pointed out the shock problem in the use of VNT that can occur at the nozzle exit under high inlet pressure conditions.

Undoubtedly, the thickness and solidity of guide vane can directly affect the turbine stage performance as well as the flow characteristic inside nozzle and rotor [23, 24]. Hence, a clear understanding of the effect of guide vane with different thickness and solidity is required for further improvement of a VNT. Current work is divided into three parts: Firstly, three guide vanes with different thickness and solidity were numerically studied at both small and large nozzle open conditions, to compare the stage performance; secondly, the characteristics of nozzle leakage flow, the entropy distribution in turbine as well as the intensity of shock of three models was analyzed in detail. Finally, the aerodynamic loading fluctuation of rotor blades due to nozzle leakage flow and shock was analyzed in detail.

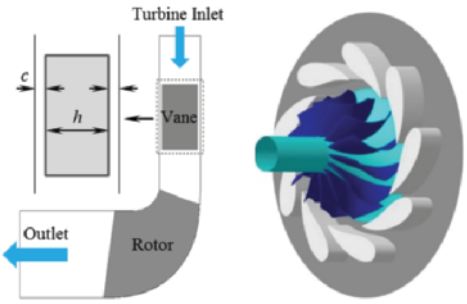

Fig. 1. Meridian and geometry structure of the base model.

2. Research methodology

The investigation has been carried out on a radial inflow turbine with variable nozzle that is used in a diesel engine turbocharger. The meridian view and geometry structure of the base model are illustrated in Fig. 1. In order to study the effect of guide vane thickness and solidity on VNT performance and aerodynamic characteristics, two new guide vanes are designed with vane count of 9 and 18, respectively, in addition to the base model with 9 vanes. The profile of base and newly designed models are shown in Fig. 2. In this work, the solidity (S) of guide vane are expressed by Eq. (1), respectively.

$$S = \frac{L_{\text{chord}}}{N_{pitch}} \tag{1}$$

where L_{chord} is the chord length and N_{pitch} is the pitch.

The main research content of this paper is the effect of thickness and solidity of guide vane on the flow and performance of VNT. Since the gap between nozzle and rotor directly affects the performance and flow characteristics of turbine [25], the three models adopted the same nozzle outlet diameter in this design to eliminate the influence of the gap. The profile of three guide vanes is shown in Fig. 2, it can be seen that the thickness of three models gradually decrease from base vane to vane B model. Meanwhile, the vane count of vane B model is increased to 18 in order to increase guide vane solidity. The VNT parameters of three models are de-fined and shown in Table 1.

2.1 Numerical method

The perfect gas was adopted in the simulations, and the commercial code EURANUS in FINE™/Turbo was used to solve the three-dimensional Reynolds-averaged Navier-Stokes

Table 1. Main parameters of the research models.

Parameters	Base	Vane A	Vane B	Rotor
Blade count	9	9	18	13
Inlet diameter/mm	122	122	122	37
Outlet diameter/mm	73.8	73.8	73.8	--
Height/mm	10.7	10.7	10.7	--
Chord/mm	41	41	41	--
Thickness/mm	12.6	6.3	4.2	--
Pitch/mm	27.9	27.9	13.95	--
Solidity	1.47	1.47	2.94	--
Trailing edge diameter/mm	1	1	1	--
Clearance/mm	0.15	0.15	0.15	0.3

(a) Base vane (b) Vane A (c) Vane B

Fig. 2. Profile of three guide vanes.

equations. The governing equations can be expressed as:

$$\frac{\partial U}{\partial t}+\nabla\vec{F_I}+\nabla\vec{F_V}=Q. \tag{2}$$

$\vec{F_I}$ and $\vec{F_V}$ are the inviscid and viscous flux vectors, respectively. Q is the source term. $\vec{F_I}$ and $\vec{F_V}$ can be further decomposed into Cartesian components as follows:

$$F_I=f_{I1}\vec{l_x}+f_{I2}\vec{l_y}+f_{I3}\vec{l_z}, \tag{3}$$

$$F_V=f_{V1}\vec{l_x}+f_{V2}\vec{l_y}+f_{V3}\vec{l_z}, \tag{4}$$

$$U=\begin{bmatrix}\overline{\rho}\\ \overline{\rho}\tilde{w}_1\\ \overline{\rho}\tilde{w}_2\\ \overline{\rho}\tilde{w}_3\\ \overline{\rho}\tilde{w}_4\end{bmatrix}, \tag{5}$$

$$F_{Ii}=\begin{bmatrix}\rho\tilde{w}_i\\ \overline{p^*}\delta_{1i}+\overline{\rho}\tilde{w}_i\tilde{w}_1\\ \overline{p^*}\delta_{2i}+\overline{\rho}\tilde{w}_i\tilde{w}_2\\ \overline{p^*}\delta_{3i}+\overline{\rho}\tilde{w}_i\tilde{w}_3\\ \left(\overline{\rho}\tilde{E}+\overline{p^*}\right)\tilde{w}_i\end{bmatrix}, \tag{6}$$

$$F_{Vi}=-\begin{bmatrix}0\\ \tau_{i1}\\ \tau_{i2}\\ \tau_{i3}\\ q_i+\tilde{w}_j\tau_{ij}\end{bmatrix}. \tag{7}$$

The Jameson's central-difference scheme and the four-stage explicit Runge-Kutta method were employed to complete the space discretization and time integration, respectively. The main reason for choosing the Spalart-Allmaras turbulence model to calculate the turbulent viscosities is that it can predicate the turbine performance well, compared with the test result at nozzle different opening conditions [26-28].

As for the boundary conditions, total pressure and total temperature were specified at the nozzle inlet; static pressure was applied at turbine outlet. All of the boundary conditions adopted in the numerical simulations corresponding to the test results in this work. In this work, the steady calculations were carried out to obtain the performance of study models; the unsteady calculations were performed to better study the flow characteristics in turbine. For steady calculations, the conservative pitchwise coupling was adopted at the R-S interface; for the unsteady calculations, a direct interpolation on two sliding surfaces of the R-S interface was used.

2.2 Grids and boundary conditions

The structured grids of computational domain were generated by IGG/Auto-grid software. The computational domain was divided into five subareas. Around guide vane and rotor blade surface, "O" type grid was used. In the end-wall clearances, "butterfly" type grid was adopted to improve the quality. "H" type grid was applied in the other subareas. Grid clustering was used around the solid wall surfaces to calculate the boundary layer and the Y^+ is less than 2.5. In present work, single passage grid was used in steady computation to predict turbine performance; multi-passage grid was applied in unsteady computation to better study the flow characteristic of turbine. In order to save computing time, the computational domain scaling method was applied in the unsteady calculations, in which the number of rotor blades was reduced from 13 to 12, thus, the ratios of Nv/Nr of the three models can be reduced to 3:4, 3:4 and 2:3, respectively. Fig. 3 shows the computational grids as well as the Y+ value distribution for all the walls of base model.

2.3 Numerical validation

The quality and number of the grid has great influence on the simulation results. In order to get accurate solution and save computation time, the grid independence study was carried out on the base model first. The grid configurations, as well as the variation of isentropic efficiency with grid numbers are presented in Table 2. It can be seen that the difference between coarse grid (case 1) and medium grid (case 2) is 0.78 %, and between medium grids and fine grid (case 3) is 0.15 %. Thereby, the medium grid was applied in the numerical simulations.

To calibrate the accuracy of the CFD method, the test of base model was carried out on a turbocharger flow bench. Fig. 4 illustrates the test equipment and instruments on the turbo-

Table 2. Grids independence validate.

	Grid	Expansion ratio	MFR	η_{is}
Case 1	960000	3.95	0.3286	0.638
Case 2	1328900	3.95	0.3281	0.643
Case 3	1585500	3.95	0.328	0.644

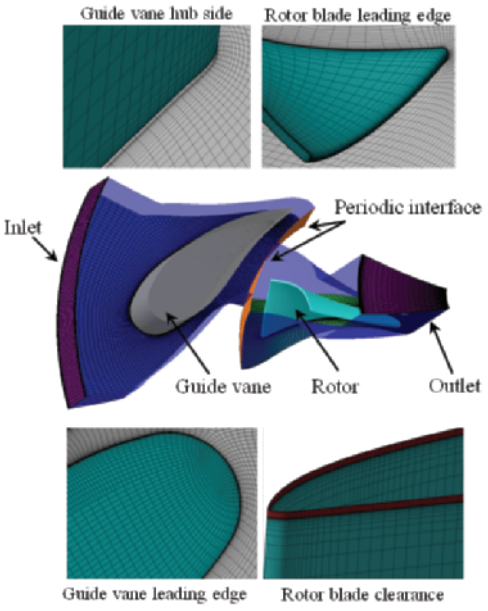

(a) Grids of the base model

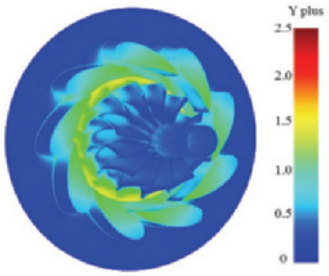

(b) Y^+ distribution in all walls for base model

Fig. 3. Grid and Y^+ distribution of base model.

charger flow bench.

The high-pressure air was heated by an electric heater to drive the base turbine. A compressor, coaxially connected with the turbine, was used to absorb the power generated by the turbine. Static pressure, total pressure and total temperature sensors were installed both at turbine inlet and outlet to acquire relevant parameters of gas. A mixer was adopted before the gas temperature was measured at the turbine outlet. The turbine housing and pipes to/from the turbine have insulation to reduce heat loss.

In addition, the oil temperature was also measured to ensure test consistency. In this test, the precision of temperature sensors is ±0.1 %. Pressure measurements are done by piezoresistive sensors with a precision of ±0.3 %. The rotor speed is measured by an external magnetic induction tachometer with a

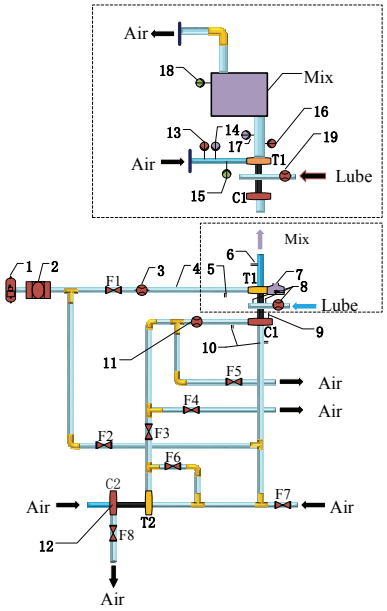

Fig. 4. Schematic of the turbine test (1. Air supply, 2. Air cleaner, 3. Flowmeter, 4. Electric heater, 5. Turbine inlet section, 6. Turbine outlet section, 7. Turbine, 8. Lubricating oil section, 9. Rotational speed meter, 10. Compressor section, 11. Flowmeter, 12. Auxiliary turbocharger, 13. Static pressure sensor, 14. Total pressure sensor, 15. Total temperature sensor, 16. Static pressure sensor, 17. Total pressure sensor, 18. Total temperature sensor, 19. Flowmeter, C1. Compressor to be tested, C2. Auxiliary compressor, T1. Turbine to be tested, T2. Auxiliary turbine, F1 to F8. Flow control valves).

precision of ±0.2 %. The isentropic efficiency of turbine can be calculated using following formula:

$$\eta = \frac{W_{T1}}{W_{T0}} = \frac{c_p\left(T_0 - T_2\right)}{\frac{k}{k-1}RT_0\left(1-\frac{1}{\pi^{\frac{k-1}{k}}}\right)}, \tag{8}$$

$$\pi = p_0 / p_2 \tag{9}$$

where W_{T1} is the actual expansion work; W_{T0} is the isentropic expansion work; T_0 and T_2 are the total temperature at turbine inlet and outlet, respectively; π is the expansion ratio of turbine; k is the specific heat ratio, k = 1.4; R is the gas constant, R = 287 J/kg K; c_p is the specific heat at constant pressure, c_p = 1006 J/kg K. p_0 is the total pressure of turbine inlet; P_2 is the static pressure of turbine outlet.

In Eq. (8), the W_{T1} can be calculated by measuring the turbine inlet temperature and the pressure at turbine inlet and outlet. In order to measure turbine outlet temperature accurately, an indirect method of measurement is adopted in this test. In which, the actual compression work of the compressor and the mechanical loss of the bearing are both measured, and the W_{T1} can be calculated by formulas below:

$$W_{T1} = W_{Cact} + W_{Oil}, \tag{10}$$

$$W_{Cact} = m_C \int_1^2 C_{p,Air} dT_C^*, \tag{11}$$

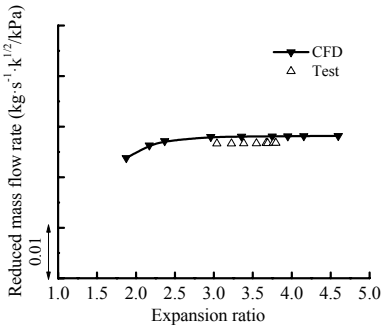

(a) Stage mass flow rate curves

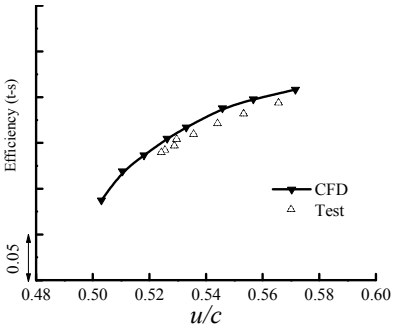

(b) Stage efficiency curves

Fig. 5. Comparison of the CFD and test results.

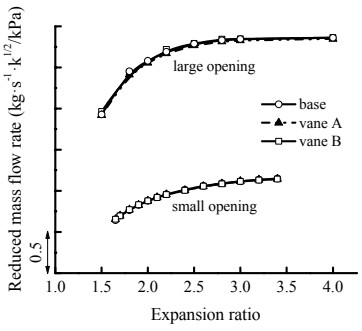

(a) Turbine stage mass flow rate curves

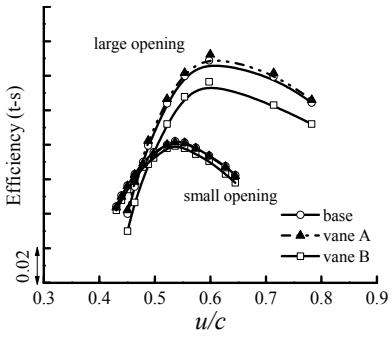

(b) Turbine stage efficiency curves

Fig. 6. Performances comparison of the three models.

$$W_{Oil} = m_{Oil}\int_{1}^{2} C_{p,Oil}dT^{*}_{Oil} \tag{12}$$

where W_{Cact} is the actual compression work of compressor; W_{Oil} is the mechanical loss of the bearing; m_C is the mass flow rate of compressor; m_{Oil} is the mass flow rate of lubricating oil; $C_{p,Air}$ is the specific heat at constant pressure of air; $C_{p,Oil}$ is the specific heat at constant pressure of lubricating oil.

Fig. 5 shows the comparison between CFD results and test data at turbine speed of 100 kr/min with nozzle design opening. Limited by the test condition, there was only a narrow range available for the comparison. It can be seen that the CFD results agree well with test data at different expansion ratios. The maximum error of stage efficiency between test and CFD is less than 2 percent; and the maximum MFR error is less than 3.5 percent. The discrepancy for the MFR is mainly due to the fact that the volute was not included in the simulation model, which means that the pressure drop between volute inlet to the inlet of computation domain was ignored thus reduced mass flow will be impacted by the difference in inlet conditions of computational/experimental domain, leading to the increase the MFR of turbine; and the stage efficiency discrepancy is possibly due to the heat and friction loss in the volute that was not captured in CFD.

3. Result and discussion

3.1 Turbine performance

Fig. 6 shows the comparison of turbine MFR and stage performance of three models under different expansion ratios at both small and large nozzle openings. Fig. 6(a) shows that as the expansion ratio increases, the MFR of three models are almost the same at two nozzle openings. Fig. 6(b) compares turbine stage efficiency of three models at both small and large nozzle opening conditions. At small nozzle opening condition, there is no obvious difference in turbine stage efficiency between the base model and vane A model at different u/c values, indicating that the thickness of guide vane has less effect on turbine performance when guide vane solidity is constant. However, with the solidi-ty increases, the efficiency of vane B model is about 0.5 % lower than the other two models with u/c values between 0.55 and 0.65 at small nozzle opening; while at large nozzle opening, the efficiency penalty reaches 1.4 % for u/c values between 0.6 and 0.8. The result indicates that the changing of thickness and solidity of guide vane has less effect on the turbine stage efficiency at small nozzle opening; while, with the increasing of nozzle opening, the effect will be enhanced.

3.2 Loading and nozzle leakage flow

Fig. 7 presents the loading distribution of guide vane on suction side (SS) and pressure side (PS) at 50 % span for three models at small nozzle opening condition. At this small operation condition, the rotor speed is 50 kr/min, the expansion ratio of turbine is 1.46 and the u/c value is 0.54.

In base model, the rapid increasing of loading from leading edge to 35 % chord position is mainly caused by the excessive

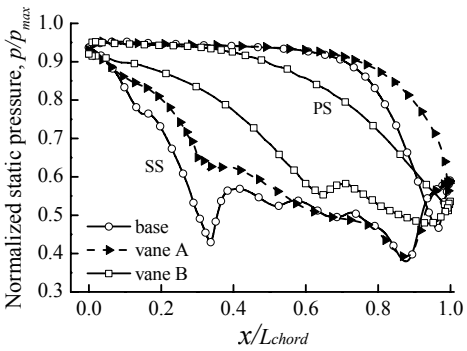

Fig. 7. Loading distributions at 50 % span for three models.

acceleration of exhaust gas. A contrast analysis of three models shows that the loading of vane A model from leading edge to about 60 % chord position is lower than that of base model, while from 60 % chord position to guide vane trailing edge the loading is higher than base model. The result indicates that when vane count is constant, decrease in the thickness of guide vane can move the loading towards trailing edge. In vane B model, due to the increased vane count, the acceleration status of exhaust gas has been greatly changed, thus the loading is much different from that in base and vane A models, which will be discussed in detail in following analysis.

Fig. 8 presents the streamline and entropy distribution on the hub side of nozzle for three models at small nozzle open condition. Since the leakage flow characteristic and entropy distribution on shroud side of nozzle is similar to that on hub side, only the flow of hub side is shown here. It can be seen that the leakage flow along guide vane chord is composed of two parts: Leakage vortex and leakage jet. The leakage vortex mainly generates at fore part of guide vane, which is due to the interaction between nozzle leakage flow and the main flow. At aft part, without the influence from the main flow, the nozzle leakage flow directly enters the rotor in a form of leakage jet. In three models, the high entropy area at nozzle downstream is mainly caused by the leakage vortex. From Fig. 8, it can also be seen that the flow characteristic and entropy distribution of vane A model is similar to that of base model. As the thickness decreases, the loading in vane A moves towards the guide vane aft part, thus the intensity of leakage vortex flow near guide vane leading edge is weakened slightly, and so does the high entropy region caused by the leakage vortex. Comparing the base model with vane B model it is found that for the base model, driven by higher loading, the separation line starts from the guide vane leading edge and runs through the whole flow field of nozzle. On the contrary, because the loading on vane B model has been decreased, the intensity of leakage vortex as well as the associated high entropy area is also weakened. The loss in vane B model is mainly caused by the leakage jet, as well as the guide vane wake. In addition, since the vane count of vane B model is double that of Base and vane A models, the total loss in three models cannot compare in Fig. 8.

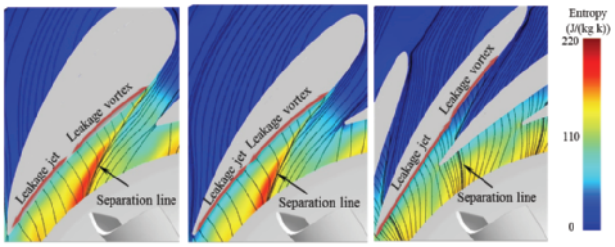

(a) Base model (b) Vane A (c) Vane B

Fig. 8. Nozzle leakage flow and limiting streamline on hub side of three models.

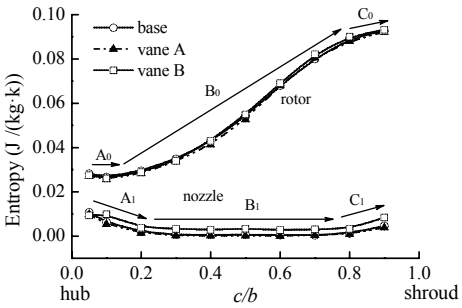

Fig. 9. Entropy distributions from 5 % to 95 % spans.

3.3 Flow loss comparison

To better estimate the loss inside turbine, the entropy of three models at different spans was obtained by the method of surface integration, which is defined as following:

$$Entropy_s = \int_s \frac{C_p}{\gamma} \log\left[\left(\frac{P_s}{P_r}\right)^{(1-\gamma)}\left(\frac{T_s}{T_r}\right)^{\gamma}\right] \cdot \left|\vec{ds}\right| \tag{13}$$

where C_P is the specific heat at constant pressure; P_s is the local pressure; P_r is the reference pressure; T_s is the local temperature; T_r is the reference temperature; s shows the integral area.

Fig. 9 shows the entropy distribution from 5 % to 90 % span of three models at small nozzle open condition with the expansion ratio of turbine is 1.46 and the u/c value is 0.54. From the comparison between nozzle and rotor it can be found that the highest entropy resides inside of rotor. Considering the entropy of nozzle, the flow loss near hub (A_1) and shroud (C_1) areas is higher than that in other span areas due to the effect of nozzle leakage flow. From 20 % to 80 % vane height (B_1), the entropy of nozzle is mainly caused by the boundary and wake losses. Due to increased vane count, the wake and boundary losses for vane B model are also increased. Thus, the entropy of vane B model in nozzle is slightly higher than the other two models. For the entropy distribution in the rotor it can be seen that from hub to shroud the value gradually increases, before it reaches the maximum at shroud side. Furthermore, the increasing rate of entropy near hub and shroud (A_0 and C_0) side is lower than that in other span areas (B_0). This phenomenon indicates that

Table 3. Area ratio in the acceleration channels.

	First channel	Second channel
Base	0.22	0.23
Vane A	0.18	0.15
Vane B	0.14	0.11

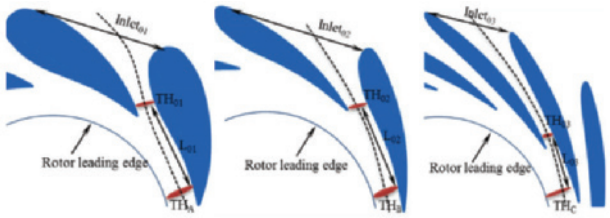

(a) Base model (b) Vane A (c) Vane B

Fig. 10. Acceleration channels schematic of three models.

at nozzle small opening, the typical separation vortex loss caused by the large incident angle of nozzle at rotor leading edge is the highest in B_0 area [6].

3.4 Exhaust gas acceleration inside nozzle

Fig. 10 presents the structure of the acceleration channels of three models at small nozzle opening. For base model, the acceleration of the exhaust gas is mainly controlled by two acceleration channels that can be regarded as two Laval nozzles [29], as shown in Fig. 10(a). As for vane B model, the position of the first throat (TH01) has been moved to trailing edge due to the changing of the profile at suction side. Meanwhile, the width of TH01 has also been enlarged slightly for vane A model, thus the area ratio between inlet and the first throat is smaller than that of the base model. As for vane B model, due to the vane count increased, the area ratio between inlet and the first throat is the smallest among the three models.

Fig. 11 shows the Mach number distribution at mid-span of three models at the *u/c* value of 0.6. As for the boundary conditions, the rotor speed is 80000 rpm and the expansion ratio of turbine is 4. For base model, the exhaust gas firstly accelerates from guide vane leading edge (Inlet01) and reaches the critical speed at the first throat (TH01). Then, the exhaust gas continues to accelerate due to the Laval nozzles structure of the first acceleration channel and a shock is generated after the first throat. After the first acceleration channel, the exhaust gas enters the second acceleration channel that is composed of the guide vane suction side and the leading edge of the rotor, and continue to accelerate. Similarly, the critical speed of the exhaust gas in the second acceleration channel appears at the second throat (THA), and the trailing edge shock is generated after the THA. It can be seen that the acceleration process of three models are different. Compared to base model, there is no supersonic flow generates inside of vane A (TH02) and vane B (TH03) models in the first acceleration channel because the area ratio between inlet and the first throat of the two

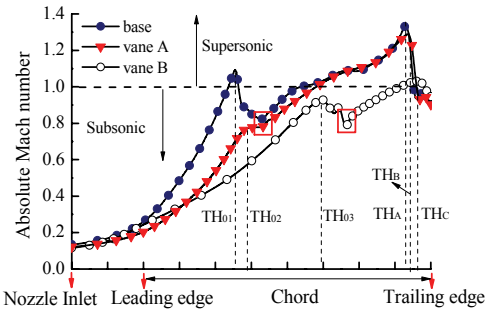

Fig. 11. Mach number at mid-span of three models.

models has been decreased, leading to a decrease in velocity.

Mach number distribution of the three models reveals that the exhaust gas has almost the same speed before accelerating in the second acceleration channel (noted by squares in Fig. 11). In the second acceleration channel, the Mach number distribution for base and vane A model is almost the same with each other. While for vane B model, the Mach number is far lower than that of base and vane A model. The gas speed of three models reaches the maximum value after the second throat position (THA, THB, THC), and obviously, the maximum speed of vane B model is much lower than that of the other two models. The phenomenon may be caused by the following reasons: (1) The number of the second throat for vane B model is increased correspondingly as the vane number increases, thus the acceleration degree of exhaust gas is mitigated; (2) the low flow velocity wake from the neighbouring vane acts as a 'wall' separating the flows in its two sides. When the solidity increases, the outlet area is greatly reduced by this 'wall' hence the gas acceleration is restricted.

The comparison of acceleration process for three models reveals that the solidity of guide vane could affect the acceleration process of the exhaust gas significantly. If the solidity is increased, the acceleration of the exhaust gas will be restricted effectively. Therefore, this method can be used in the guide vane design process to weaken shock.

3.5 Shock

At engine exhaust braking conditions, turbine usually works at small nozzle opening with high backpressure conditions. In case the acceleration of exhaust gas reaches critical condition, shock will be induced between the guide vane throat and trailing edge area [19, 20]. Fig. 12 shows the static pressure distribution with isoline at 50 % vane height of three models. It can be seen that there is a rapid static pressure change corresponding to the areas of dense isoline, indicating that shock has been generated in this region. The higher the shock intensity, the more crowded the isoline. Through the contrastive analysis of the isoline density it can be found that the intensities of shock in both the base model and vane A model are higher than that in vane B model. In additional to shock at 50 % vane height, a phenomenon should be pointed out that due to the

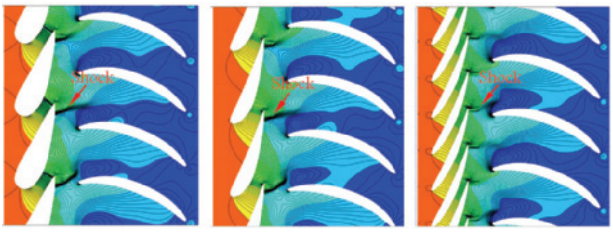

(a) Base model (b) Vane A (c) Vane B

Fig. 12. Shock at nozzle outlet of three models.

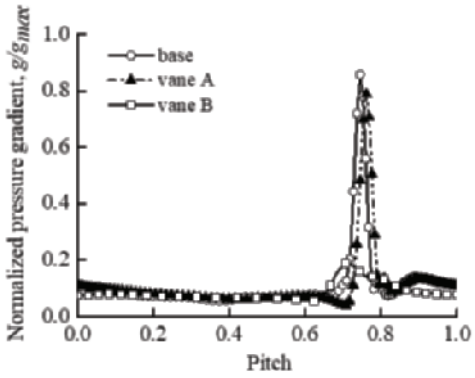

Fig. 13. Intensity of shock for three models at nozzle outlet.

impact of the relative position between rotor and stator, the shocks also change in shape and strength.

Fig. 13 shows the static pressure gradient distribution of the three models. To make quantitative analysis of the shock intensity, the static pressure gradient was analyzed. The pressure gradient is defined as following:

$$grd(p) = \frac{d\mathrm{p}(\theta)}{d\theta} \tag{14}$$

where p is the static pressure and θ is the angle along circumferential direction.

A contrast analysis indicates that the intensity of shock for the base model is almost the same as that of the vane A model, and the difference between the two is less than 5 percent. Compared to the base model and vane A model, however, the intensity of shock in vane B model decreases by about 75 %. The results show that the vane number has significant effect on the intensity of shock; with the solidity increasing, the shock can be weakened effectively.

3.6 Non-uniformity flow of rotor inlet

In general, nozzle leakage flow could lead to non-uniformity flow of rotor leading edge, which may contribute to high-cycle failure of rotor blades. Fig. 14 presents the Mach number distribution of three models at 5 % span when the expansion ratio of turbine is 4 and the u/c value is 0.6. It is found that the flow field of rotor inlet for the base model and vane A model is composed of three parts: Main flow (A), leakage vortex flow (B) and

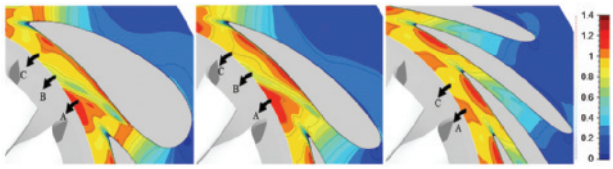

(a) Base model (b) Vane A model (c) Vane B model

Fig. 14. Mach number at 5 % span of three models.

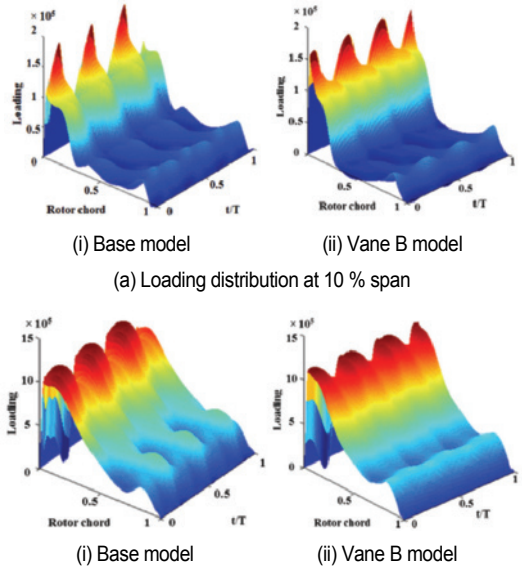

(i) Base model (ii) Vane B model

(a) Loading distribution at 10 % span

(i) Base model (ii) Vane B model

(b) Loading distribution at 50 % span

Fig. 15. Loading distribution of the rotor blade at 10 % and 50 % span.

leakage jet flow (C). After the interaction with the leakage vortex flow, the main flow enters the rotor at A position with the maximum velocity. The leakage vortex flow, dissipated along the flow path, enters rotor with the minimum velocity and causes the non-uniformity flow field at rotor inlet. The velocity of leakage jet flow, unaffected by main flow, is between the velocity of leakage vortex and the main flow. For the vane B model, unaffected by leakage vortex flow, there only exist main flow and leakage jet flow at the rotor inlet. Comparison of three models at 5 % span reveals that the base model and vane A model have similar velocity distribution, representing a more severe non-uniformity than that of vane B model. Thereby, increasing the guide vane count can effectively mitigate the intensity of leakage vortex, thus decrease the non-uniformity flow field at rotor inlet position.

3.7 Loading fluctuation of rotor blade

The shock and nozzle leakage flow periodically impinge on the rotor blades, often raising HCF concerns of turbine. In this section, the aerodynamic loading fluctuation on rotor blade surface will be discussed in detail. In order to highlight the effect of shock and nozzle leakage flow on the downstream rotor, the spatial and temporal loading fluctuation of base and vane B model at 10 % and 50 % spans of rotor blade were illustrated

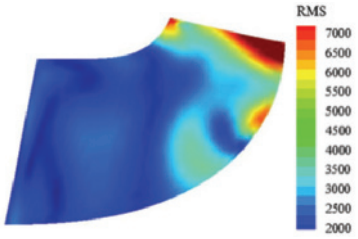

(a) Base model

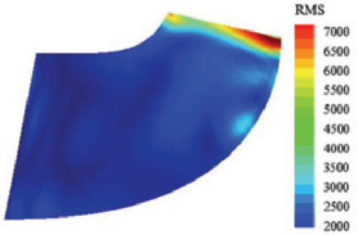

(b) Vane B model

Fig. 16. Static pressure f_{rms} of rotor blade suction surface.

in Fig. 15. Since the intensity of nozzle leakage flow and shock of base model is almost the same as that of the vane A model, therefore only the base and vane B model were compared. From the comparison of the following pictures it is found that the loading spikes of two models appear at the rotor leading edge position. As for the boundary conditions, the rotor speed is 80000 rpm, the expansion ratio of turbine is 4 and the *u/c* value is 0.6.

At 50 % span, because of the high intensity shock, the maximum loading as well as the fluctuation amplitude of the base model is larger than that of vane B model. The maximum value for base model is 15 where for the vane B mode, the value is 13. Similar phenomenon was also found at 10 % span, which is mainly due to the fact that the intensity of nozzle leakage flow of base model is larger than vane B model. The maximum value of base model is 2 and for the vane B mode, the value is 1.85. This phenomenon clearly shows that the increasing of guide vane solidity can effectively weaken the intensity of aerodynamic loading amplitude of rotor blades, thus decrease the risk of HFC of rotor blades.

To analyze the intensity of aerodynamic loading fluctuation on rotor blade quantitatively, the static pressure root mean square value (f_{rms}) is introduced and defined as follows:

$$f_{rms} = \sqrt{\frac{1}{n}\sum_{i=0}^{n-1}\left(p_{i,t} - p_{ave,t}\right)^2} \tag{15}$$

where $p_{i,t}$ is the pressure at time t; $p_{ave,t}$ is the average pressure for all the time steps.

Fig. 16 shows the f_{rms} distribution on rotor blade suction side of the two models. It is found that the area with high intensity of loading fluctuation mainly is near the blade leading edge, which corresponds to the position where the rotor blade fracture occurred in a practical application [12]. The intensity of loading fluctuation gradually decreases along the chord from blade leading to trailing edge. Compared to the base model, it can be found that the high f_{rms} areas of vane B model shrinks effectively as the intensity of shock and nozzle leakage flow is weakened, especially at the hub side. The result further confirms that the guide vane with small thickness and large vane count can effectively shrink the high loading fluctuation areas of rotor blade, thus the aerodynamic excitation of rotor blade will be mitigated significantly, which may be very helpful to reduce the risk of HCF and hence enhance the reliability of rotor blades.

4. Conclusions

The effect of the thickness and solidity of guide vane on the stage performance as well as the flow characteristic for a radial inflow turbine with variable nozzle are investigated in detail, and the main conclusions are as following:

(1) The newly designed low thickness and high solidity nozzle (vane B) reduces shock by 75 % compared to the base nozzle; meanwhile, it can also mitigate the nozzle end-wall leakage flow thus improves the flow uniformity of rotor inlet. As a result, the loading fluctuation and HCF risk of the wheel can be reduced, which is beneficial to the reliability of turbine.

(2) At small nozzle opening, the newly designed nozzle only shows about 0.5 % lower efficiency than the base model; at large open condition, the efficiency degradation of the newly designed nozzle is up to 1.5 %. Therefore, there is a trade-off between the efficiency and forced response when choosing the nozzle vane solidity and thickness.

(3) From the comparison of the shock intensity and the performance of the three models, we recommend that a suitable guide vane can be selected according to the common working condition of engine. If the VNT does not often work at the maximum open, the guide vane with low thickness and high solidity should be adopted to weaken the intensity of shock as well as to mitigate the aerodynamic excitation of rotor blade.

Acknowledgments

This work was supported by the National Natural Science Foundation of China (Grant/Award Number: '51576015') and the Fundamental Research Funds for the Central Universities (Grant/Award Number: 'N182303033').

Nomenclature

VNT	: Variable nozzle turbine
MFR	: Mass flow rate
CFD	: Computational fluid dynamics
S	: Solidity
u	: Circumferential velocity at rotor inlet
u/c	: Velocity ratio of turbine
N_v	: Number of guide vane
N_r	: Number of rotor blade

π : Expansion ratio
L_{chord} : Guide vane chord length
N_{pitch} : Pitch
h : Height of nozzle
t-s : Total to static
η : Isentropic efficiency
C_p : Specific heat at constant pressure
s : Area of zone
$TH_{01,02...}$: The first throat of nozzle
$TH_{A,B...}$: The second throat of nozzle
$p_{ave,t}$: Average pressure of all time steps
MACH : Mach number
HCF : High-cycle fatigue
f_{rms} : Root mean square value

References

[1] J. G. Hawley, F. J. Wallace, A. Cox, R. W. Horrocks and G. L. Bird, Variable geometry turbocharging for lower emissions and improved torque characteristics, *Proc IMechE, Part D, J Automobile Engineering,* 213 (1999) 145-159.

[2] A. Hishikawa, Y. Okazaki and P. Busch, Developments of variable area radial turbine for small turbochargers, *SAE Technical Paper,* 880120 (1988).

[3] G. O'Connor and M. Smith, Variable nozzle turbochargers for passenger car applications, *SAE Technical Paper,* 880121 (1988).

[4] A. T. Simpson, S. W. T. Spence and J. K. Watterson, A comparison of the flow structures and losses within vaned and vaneless stators for radial turbines, *Trans ASME, J. Turbomach,* 131 (2009) 247-254.

[5] H. Zhang, D. Lao, C. Yang and X. Wang, Internal flow characteristics of a variable mixed flow turbine with partially-rotating vane nozzle, *Journal of Mechanical Science and Technology,* 31 (10) (2017) 4977-4987.

[6] H. Tamaki, S. Goto, M. Unno and A. Iwakami, The effect of clearance flow of variable area nozzles on radial turbine performance, *ASME Turbo Expo 2008: Power for land, sea, and air,* Berlin, Germany (2008) 1519-1529.

[7] L. Hu, C. Yang, H. Sun, J. Zhang and M. Lai, Numerical analysis of nozzle clearance effect on turbine performance, *Chin J. Mech. Eng.,* 24 (4) (2011) 618-625.

[8] S. Spence, J. O'Neill and G. Cunningham, An investigation of the flow field through a variable geometry turbine stator with vane end-wall clearance, *Proc. IMechE, Part A: J. Power and Energy,* 220 (8) (2006) 899-910.

[9] J. Walkingshaw, S. Spence, J. Ehrhard and D. Thornhill, A numerical study of the flow fields in a highly off-design variable geometry turbine, *ASME Turbo Expo 2010: Power for land, sea, and air,* Glasgow, UK (2010) 1951-1960.

[10] X. W. Qiu, R. A. Mark and C. B. Nicholas, Meanline modeling of radial inflow turbine with variable area nozzle, *ASME Turbo Expo 2009: Power for land, sea, and air,* Orlando, Florida, USA (2009) 1185-1191.

[11] H. Hayami, Y. I. Hyun, Y. Senoo and M. Yamaguchi, Effects of tip clearance of nozzle vanes on performance of radial turbine rotor, *Trans. ASME, J. Turbomach.,* 112 (1990) 58-63.

[12] L. Hu, H. Sun, J. Yi, E. Curtis and J. Zhang, Investigation of nozzle clearance effects on a radial turbine: Aerodynamic performance and forced response, *SAE Technical Paper,* 2013-01-0918 (2013).

[13] Y. Liu, C. Yang, M. Qi, H. Zhang and B. Zhao, Shock, leakage flow and wake interactions in a radial turbine with variable guide vanes, *ASME Turbo Expo 2014: Power for Land, Sea, and Air,* Düsseldorf, Germany (2014).

[14] A. Kulkarni and G. Larue, Vibratory response characterization of a radial turbine wheel for automotive turbocharger application, *ASME Turbo Expo 2008: Power for land, sea, and air,* Berlin, Germany (2008) 583-591.

[15] A. T. Simpson, Numerical and experimental study of the performance effects of varying vaneless space and vane solidity in radial turbine stators, *Journal of Turbomachinery,* 135 (3) (2013) 420-431.

[16] D. Yang, C. Yang, L. Hu, J. J. Yi, E. Curtis and M. S. Wooldridge, Numerical investigation of the split sliding guide vane for a variable nozzle turbine, *Proc. IMechE, Part D, J. Automobile Engineering,* 233 (8) (2018) 2074-2084.

[17] M. Qi, X. Lei, Z. Wang and C. Ma, Investigation on the flow characteristics of a VNT turbine under pulsating flow conditions, *Proc. IMechE, Part D, J. Automobile Engineering,* 233 (2) 396-412.

[18] B. Zhao, M. Qi, H. Sun and S. Xin, Variable nozzle turbocharger turbine performance improvement and shock wave alternation by distributing nozzle end-wall clearances, *Proc. IMechE, Part D, J. Automobile Engineering,* 233 (8) 1971-1981.

[19] H. Chen, Turbine wheel design for Garrett advanced variable geometry turbines for commercial vehicle applications, *Proc. 8th International Conference of Turbochargers and Turbocharging,* London (2006) 317-327.

[20] T. Kawakubo, Unsteady rotor-stator interaction of a radial-inflow turbine with variable nozzle vanes, *ASME Turbo Expo 2010: Power for Land, Sea, and Air,* Glasgow, UK (2010) 2075-2084.

[21] D. F. Yang, D. Z. Lao, C. Yang, L. Hu and H. Sun, Investigations on the generation and weakening of shock wave in a radial turbine with variable guide vanes, *ASME Turbo Expo 2010: Power for Land, Sea, and Air,* Seoul, South Korea (2016).

[22] A. J. Feneley, A. Pesiridis and A. M. Andwari, Variable geometry turbocharger technologies for exhaust energy recovery and boosting - A review, *Renewable and Sustainable Energy Reviews*, 71 (2017) 959-975.

[23] D. X. Zhu, *Turbocharging and Turbochargers,* Beijing: China Machine Press (1992).

[24] Y. R. Ganesh, S. B. Siddharth and V. K. Keerthi, Numerical investigation: Effect of stator vanes on turbocharger turbine performance, *Int. J. Rotating Mach.,* 2014 (2014).

[25] J. Walkingshaw, S. Spence, J. Ehrhard and D. Thornhill, An experimental assessment of the effects of stator vane tip clearance location and back swept blading on an automotive vari-

able geometry turbocharger, *Trans. ASME, J. Turbomach.,* 136 (6) (2013).
[26] X. C. Zhu, P. Y. Liu, J. G. Chen, X. Shen and Z. H. Du, Reduced-order modelling of wind turbine airfoil unsteady aerodynamic loading, *Proc. IMechE, Part A: J. Power and Energy,* 229 (1) (2015) 24-32.
[27] G. Han, X. G. Lu, Y. F. Zhang, S. F. Zhao, C. W. Yang and J. Q. Zhu, Investigation of two pipe diffuser configurations for a compact centrifugal compressor, *Proc. IMechE, Part G: J. Aerospace Engineering* (2017) 1-13.
[28] K. Chandler, A. White and J. Young, Non-equilibrium wet-steam calculations of unsteady low-pressure turbine flows, *Proc IMechE, Part A: J. Power and Energy,* 228 (2) (2014) 143-152.
[29] D. F. Yang, D. Z. Lao, C. Yang, L. Hu and H. Sun, Design and numerical analysis of a forepart rotation vane for a variable nozzle turbine, *International Journal of Turbo & Jet-Engines,* 36 (3) 233-244.

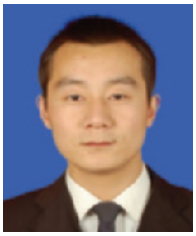

Dengfeng Yang obtained his Ph.D. degree from Power Machinery and Engineering from Beijing institute of Technology (BIT), and is currently working at Northeastern University at Qinhuangdao, China. His research interests include radial/mixed turbine design and the complex flow in turbomachinery.

Dazhong Lao is an Associate Professor in School of Aerospace Engineering, Beijing Institute of Technology (BIT). He received the Ph.D. degree from the Dalian University of Technology in 1995. His current research interest is turbomachinery aerodynamics.